INSTITUTE OF PHYSICS PUBLISHING PLASMA SOURCES SCIENCE AND TECHNOLOGY

Plasma Sources Sci. Technol. **12** (2003) 561–575 PII: S0963-0252(03)66965-3

H- to W-mode transitions and properties of a multimode helicon plasma reactor

Ronald L Kinder[1,4], **A R Ellingboe**[2] **and Mark J Kushner**[3,5]

[1] University of Illinois, Department of Nuclear Engineering, 1406 W. Green St., Urbana, IL 61801, USA
[2] Plasma Research Laboratory, School of Physical Sciences, Dublin City University, Dublin 9, Ireland
[3] University of Illinois, Department of Electrical and Computer Engineering, 1406 W. Green St., Urbana, IL 61801, USA

E-mail: ron.kinder@novellus.com, bert.ellingboe@dcu.ie and mjk@uiuc.edu

Received 9 December 2002, in final form 28 July 2003
Published 5 September 2003
Online at stacks.iop.org/PSST/12/561

Abstract
Magnetically enhanced inductively coupled plasmas (MEICPs) typically display mode jumps as power or the magnetic field is increased. Inductive (H-mode) to helicon (W-mode) transitions in research reactors having uniform axial magnetic fields are often accompanied by a change in the spatial model structure and rapid increase in plasma density. In industrial plasma sources, the magnetic field structure is often non-uniform, producing less pure modal structure and transitions. In this paper, the characteristics of research and industrial MEICPs are computationally investigated using results from a three-dimensional plasma equipment model. When excluding the electrostatic term in the solution of Maxwell's equations, experimental observations for mode structure and transitions from H- to W-mode in the research reactor are reproduced and occur coincident with the formation of shorter axial wavelength modes, radial modes and the onset of rotation of the electric fields. Similar scaling laws were observed in the industrial reactor having a flaring magnetic field. Simultaneous H- and W-mode behaviour occurred (as characterized by radial modes and rotation of the electric field) in different regions of the plasma source depending on the local value of the helicon wavelength. When including the electrostatic terms in the solution of Maxwell's equations, more power deposition occurs in the periphery of the reactor and the H- to W-mode transition occurs at lower powers.

1. Introduction

Magnetically enhanced inductively coupled plasmas (MEICPs), of which helicons are one variety, are of interest due to their ability to deposit power in the volume of high plasma density systems ($>10^{11}$–10^{12} cm^{-3}) beyond the confines of the classical skin depth [1–3]. A typical MEICP reactor has a static solenoidal magnetic field and radio frequency (rf) antenna whose axial and azimuthal segments in part determine the mode structure of the resulting electromagnetic fields in the plasma. Although numerous previous studies have investigated the basic mechanisms of operation of MEICPs and helicons [4, 5], there is still an ongoing discussion as to the dominant methods of power deposition, particularly as to those responsible for mode jumps which accompany local increases in plasma density [6, 7]. Proposals have been made that electron Landau damping, electrostatic wave damping (including Trivelpiece–Gould [TG] waves) and ion Landau damping play important roles [7–14].

In simple cylindrical geometries and uniform axial magnetic fields, the axial wavelength of the fundamental helicon wave ($m = 1$) is given by [15]

$$\lambda_{z1} = \frac{3.83}{R}\frac{B_o}{q\mu_o n_e \nu_{rf}}, \qquad \lambda_{z2} = \left(\frac{2\pi B_o}{q\mu_o n_e \nu_{rf}}\right)^{1/2}, \quad (1)$$

[4] Present address: Novellus Systems, 4000 North First Street, San Jose, CA 95134, USA.
[5] Author to whom any correspondence should be addressed.

where B_o is the axial magnetic field, R is the radius of the plasma volume, ν_{rf} is the rf electromagnetic frequency, n_e is the electron density, q is the elementary charge and μ_o is permeability. The terms λ_{z1} and λ_{z2} are the axial wavelengths in the low electron density limit ($n_e < 10^{12}\,cm^{-3}$ for typical plasma processing conditions) and high electron density limit ($n_e > 10^{12}\,cm^{-3}$). The fact that λ_z increases with B_o, and decreases with ν_{rf} and power deposition (presuming that n_e scales with power) in large part determines the spatial characteristics of the wave structure and power deposition in a finite sized reactor. For example, operating conditions which produce $\lambda_z < L$, where L is the length of the reactor are likely to result in multiple travelling waves which are absorbed before reaching boundaries. Conditions which produce $\lambda_z > L$ are likely to generate lower order standing waves. These scaling laws generally apply to simple narrow cylindrical geometries with uniform axial magnetic fields, and so do not strictly describe industrial reactors. Even in relatively simple geometries these scaling laws may not always hold. For example, Keiter *et al* [11] found that for constant power deposition, λ_z is only a weak function of ν_{rf} for low frequencies (<11 MHz) and increases at higher frequencies (Ar, 3–10 mTorr, 800 G, 1 kW). Kwak *et al* [12] found that n_e generally increases with frequency for constant power, implying a nearly constant λ_z.

Ellingboe and Boswell [16] investigated the modal structure of helicon plasmas sustained in argon produced by a double-half-turn antenna. They identified three modes of operation; capacitive, inductive and helicon-wave, corresponding to low, intermediate and high power deposition. At low power, ($n_e < 10^9\,cm^{-3}$), the classical skin depth is large and the plasma conductivity is low. There is little shielding of the electromagnetic fields, and so capacitive coupling from the antenna dominates (E-mode). As the skin depth decreases to fit inside the vessel with increasing plasma density, the plasma produced currents shield the imposed electromagnetic field resulting in inductive coupling (H-mode). In the presence of an axial static magnetic field, the cross field conductivity is small, thereby enabling the E_r and E_θ to penetrate into the core of the plasma. It is these components which couple to the helicon wave (W-mode). E_z, on the other hand, has a large conductivity along the field lines and does not penetrate far, largely producing power deposition on the periphery of the plasma. When E_z does penetrate into the plasma, resonant wave-particle acceleration of electrons may occur resulting in resonant wave heating. In the H-mode, the B_r and B_θ components were found to penetrate the plasma, and their radial and axial structure are consistent with propagating helicon waves. In the W-mode, the B_z component of the antenna again penetrates the plasma column, with the axial and radial structure of a propagating helicon wave. In the H-mode, the downstream radial plasma density profiles [17] had maxima at large radii, suggestive of power deposition on the plasma boundary. This is consistent with TG-mode coupling [18]. In the W-mode, a broad central peak in plasma density appears, consistent with helicon wave coupling into the bulk plasma. Modelling this bulk power deposition is the focus of this work.

In this paper, power deposition and electromagnetic mode structure in MEICP reactors are investigated using a three-dimensional plasma equipment model. A research reactor and an industrial reactor based on designs commonly used in plasma materials processing are investigated. The goals of this investigation are to characterize the modal structure of the electromagnetic field, power deposition and ion fluxes while varying B_o, ν_{rf} and power deposition. Electrostatic terms in the solution of Maxwell's equations are not included for most cases to isolate the effects of the H- to W-mode transitions. The model is evaluated by comparing predictions of the model for transitions from H-mode to W-mode to experiments performed in the research reactor. We find that in both reactors the mode structure, even for highly asymmetric magnetic fields, can generally be characterized by the ratio $\gamma = \lambda_z/L$. Large values of γ produce lower order radial and axial modes while small values of γ produce higher order radial and axial modes. The H- to W-mode transitions were associated with the onset of radial modal structure. Mixed H- and W-modes were observed in the industrial reactor. In cases where the electrostatic terms are included in the solution of Maxwell's equations, there is more power deposition in the periphery of the reactor, the helicon mode damping length is shortened and, in some cases, the H- to W-mode transition occurs at a lower power. The model used in this investigation is described in section 2. The results of our investigations when excluding the electrostatic terms are summarized in sections 3 and 4, and when including those terms in section 5. Our concluding remarks are in section 6.

2. Description of the model

The model used in this study is the three-dimensional analogue of two-dimensional model described in [19, 20]. The model, HPEM-3D, is a hybrid simulation in which the electromagnetic fields, electron energy transport and mass transport are addressed in separate modules which are iterated to a harmonic steady state. The model geometry is cylindrical (r, θ, z) and is discretized on a structured mesh. The equations which are solved are the following.

2.1. Static magnetic field

The static magnetic field, $\vec{B}$, is obtained from the vector potential $\vec{A}$,

$$\nabla \times \frac{1}{\mu}\nabla \times \vec{A} = \vec{j}_c, \qquad \vec{B} = \nabla \times \vec{A}, \tag{2}$$

where $\vec{j}_c$ is the current density in reactor surrounding solenoids and μ is the local permeability. In the cases discussed here, the solenoids exclusively pass current in the azimuthal direction and so the resulting static magnetic field components are in the (r, z) directions. We solved for the vector potential as a boundary value problem using the method of successive-over-relaxation. The numerical mesh was extended to dimensions twice that shown in figure 1 and $\vec{A} = 0$ was enforced on the boundaries.

2.2. Electromagnetics

Three components of the complex electric field $\vec{E}(r, \theta, z)$ are obtained from solution of the wave equation in the

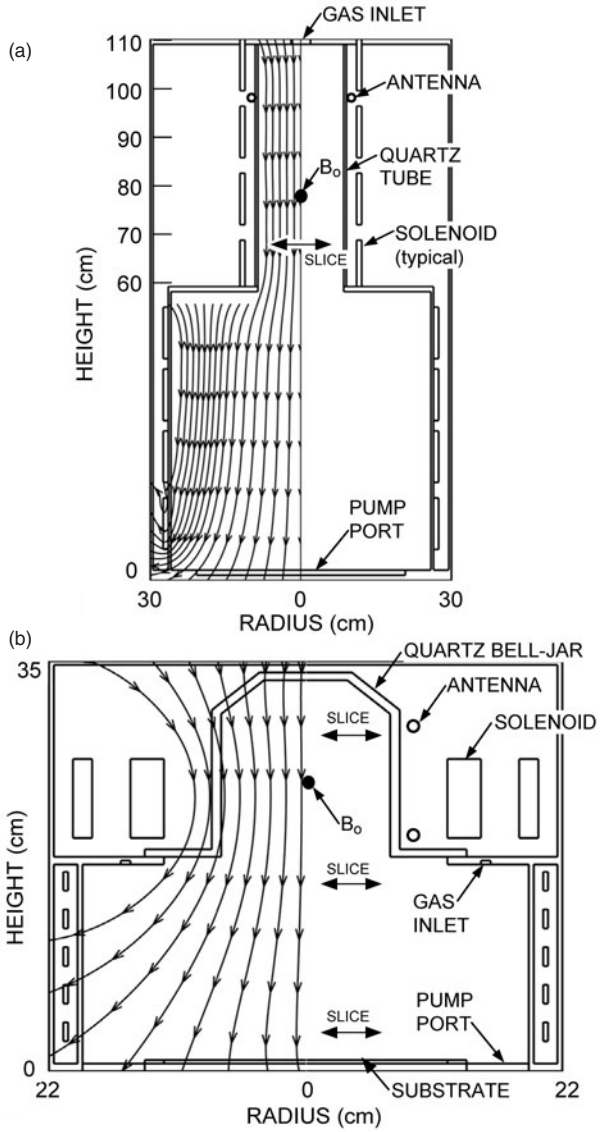

Figure 1. Schematic of the helicon reactors used in this study. (*a*) Idealized WOMBAT reactor having a uniform axial magnetic field in the upper plasma chamber of diameter 18 cm, transitioning to a downstream diffusion chamber of diameter 60 cm. The reactor is driven by a double half-turn antenna with radial feeds at $\theta = 0$ and π. The streamlines on the left panel show the static magnetic field produced by the solenoids. The point labelled B_o is the reference for magnitudes of magnetic fields. The 'observation' plane is denoted by the double arrows. (*b*) The idealized industrial reactor is azimuthally symmetric with the exception of the Boswell type antenna. The streamlines on the left panel show the static magnetic field produced by the solenoids. The double-arrows show the location of axial slices for which results will be shown ($z = 2$, 17 and 31 cm). The point labelled B_o is the reference for magnitudes of magnetic fields. The azimuthal breaks between the two segments of the antenna are at $\theta = 0$ and π.

frequency domain,

$$\nabla\left(\frac{1}{\mu}\nabla\cdot\bar{E}\right) - \nabla\cdot\left(\frac{1}{\mu}\nabla\bar{E}\right) + \omega^2\varepsilon^2\bar{E} = \mathrm{i}\omega(\bar{J} + \bar{\bar{\sigma}}\cdot\bar{E}), \tag{3}$$

where $\bar{J}$, ω, ε and $\bar{\bar{\sigma}}$ are the external antenna current density, angular electromagnetic frequency, permittivity and tensor conductivity, respectively. The tensor conductivity is given by

$$\bar{\bar{\sigma}} = \frac{qn_e}{\alpha}\frac{1}{\alpha^2 + |\vec{B}|^2} \times \begin{pmatrix} \alpha^2 + Br^2 & \alpha Bz + BrB_\theta & -\alpha B_\theta + BrBz \\ -\alpha Bz + BrB_\theta & \alpha^2 + B_\theta^2 & \alpha Br + B_\theta Bz \\ \alpha B_\theta + BrBz & -\alpha Br + B_\theta Bz & \alpha^2 + Bz^2 \end{pmatrix},$$
$$\alpha = \frac{m_e}{q}(\nu_e + \mathrm{i}\omega), \tag{4}$$

where B_r, B_θ, B_z, m_e and ν_e are, respectively, the radial, azimuthal and axial static magnetic field components, electron mass and electron momentum transfer collision frequency. The ion current in solution of equation (3) is ignored due to the low mobility of ions. We set $\nabla\cdot\vec{E} = 0$ in the majority of cases discussed here and so ignored the consequences of the electrostatic TG mode on plasma heating. The rationale was that the focus of this study is to investigate the propagation and coupling mechanisms of the inductive and helicon components of the wave. We included the electrostatic terms in a limited number of cases for comparison. Due to the far-field behaviour of the solution of equation (3) and the short wavelength structure encountered here, conventional successive-over-relaxation and conjugate gradient methods were not sufficient for its solution. The final solution method used an iterative sparse matrix technique with a quasi-minimal residual method. The routines implemented the coupled two term recurrence variants of the look-ahead Lanczos algorithms and the solution of linear systems with a quasi-minimal residual method [21].

2.3. Electron energy transport

The average electron energy is obtained from a steady state solution of the third moment of Boltzmann's equation,

$$\nabla\cdot(\bar{\bar{\kappa}}\cdot\nabla T_e) + \nabla\cdot(\Gamma_e\bar{\varepsilon}) = P_H - P_L, \tag{5}$$

where $\bar{\bar{\kappa}}$ is tensor thermal conductivity having a form analogous to equation (4), T_e is the electron temperature, $\bar{\varepsilon} = \frac{3}{2}kT_e$ is the average electron energy, Γ_e is the electron flux, P_H is the electron heating due to power deposition and P_s is the power loss due to collisions. P_H is computed from the time averaged value of $\vec{j}\cdot E$, where $\vec{j} = \bar{\bar{\sigma}}\cdot\vec{E}$. Transport coefficients as a function of average electron energy are obtained by parametrizing a two-term spherical harmonic solution of the zero-dimensional Boltzmann's equation for the electron energy distribution and constructing lookup tables which are interpolated during execution of the model. We acknowledge that previous studies have shown that there is significant non-local behaviour to the electron energy distribution which is not captured by this methodology, and which could not be addressed without greatly increasing the complexity of the three-dimensional model [20, 22, 23]. Transit time heating is highly non-linear and dependent on the time history of the electron energy distribution [16, 17, 23, 24]. We nevertheless expect that the results we discuss here are acceptable approximations of the trends.

2.4. Species density, momenta and energy

The fluid continuity, momentum and energy equations are integrated in time to provide species densities, fluxes and temperatures, and Poisson's equation is solved for the electrostatic potential. The species densities are derived from the continuity equation,

$$\frac{\partial N_i}{\partial t} = -\nabla \cdot \Gamma_i + S_i, \tag{6}$$

where N_i, Γ_i and S_i are the density, flux and source for species i. The flux for electrons is obtained using a drift-diffusion formulation to enable a semi-implicit solution of Poisson's equation, described below. The electron flux is given by

$$\vec{\Gamma}_\mathrm{e} = \bar{\bar{\mu}}_\mathrm{e} \cdot \left(q_\mathrm{e} N_\mathrm{e} \vec{E}_\mathrm{s} - \frac{kT_\mathrm{e}}{|q_\mathrm{e}|} \nabla N_\mathrm{e} \right), \tag{7}$$

where $\bar{\bar{\mu}}_\mathrm{e}$ is the electron tensor mobility having a form analogous to equation (4) and $\vec{E}_\mathrm{s}$ is the electrostatic field. Fluxes for heavy particles (neutrals and ions) are individually obtained from their momentum equations,

$$\begin{aligned}\frac{\partial \Gamma_i}{\partial t} = & -\frac{1}{m_i}\nabla (N_i k T_i) - \nabla \cdot (N_i \bar{v}_i \bar{v}_i) + \frac{q_i}{m_i} N_i (\bar{E}_\mathrm{s} + \bar{v}_i \times \bar{B}) \\ & - \nabla \cdot \bar{\bar{\eta}}_i - \sum_j \frac{m_\mathrm{j}}{m_i + m_\mathrm{j}} N_i N_\mathrm{j} (\bar{v}_i - \bar{v}_\mathrm{j}) \nu_{ij},\end{aligned} \tag{8}$$

where T_i is the temperature, $\bar{v}_i$ is velocity, $\bar{\bar{\eta}}_i$ is the viscosity tensor (used only for neutral species) and ν_{ij} is the collision frequency between species i and species j. The heavy particle temperature is determined by solving the energy equation,

$$\begin{aligned}\frac{\partial (N_i c_i T_i)}{\partial t} = & \nabla \cdot \kappa \nabla T_i - P_i \nabla \cdot \vec{\mathrm{v}}_i - \nabla \cdot (N_i \vec{\mathrm{v}}_i \varepsilon_i) \\ & + \frac{N_i q_i^2 \nu_i}{m_i (\nu_i^2 + \omega^2)} E^2 + \frac{N_i q_i^2}{m_i \nu_i} E_\mathrm{s}^2 + \sum_j 3 \frac{m_{ij}}{m_i + m_j} \\ & \times N_i N_j \nu_{ij} k_B (T_j - T_i) \pm \sum_j \tfrac{3}{2} N_i N_j R_{ij} k_B T_j,\end{aligned} \tag{9}$$

where c_i is the heat capacity, κ_i is the thermal conductivity, P_i is the partial pressure and R_{ij} is rate coefficient for formation of the species by collisions between heavy particles. There are heating contributions for charged particles from both the electrostatic and electromagnetic fields.

The electrostatic field is obtained from a semi-implicit solution of Poisson's equation. The potential for use at time $t + \Delta t$, Φ, is obtained from an estimate of the charge density at that time which consists of the charge density ρ_o at time t, incremented by the integral of the divergence of fluxes and sources over the next time interval,

$$\begin{aligned}-\nabla \cdot \varepsilon \nabla \Phi = \rho_\mathrm{o} + \Delta t \frac{\mathrm{d}\rho}{\mathrm{d}t} = \rho_\mathrm{o} - \Delta t \sum_i q_i \nabla \cdot \Gamma_i \\ - \Delta t q_\mathrm{e} \nabla \cdot \left(\bar{\bar{\mu}}_\mathrm{e} \cdot \left(-q_\mathrm{e} N_\mathrm{e} \nabla \Phi - \frac{kT_\mathrm{e}}{|q|} \nabla N_\mathrm{e} \right) \right) + \Delta t \sum_i q_i S_i.\end{aligned} \tag{10}$$

The first sum is over the divergence of ion fluxes (as obtained from equation (8)). The following term accounts for the electron flux and contains the potential, thereby making the solution implicit. The last term accounts for sources of charge due to collisions. Equation (10) is solved using the method of successive-over-relaxation.

As we have assumed that antenna coupling is purely inductive, we will not be able to resolve capacitive coupling from the antenna. At best, we will resolve transitions between H- and W-modes, but not between E- and H-modes.

3. Characteristics of MEICPs: the WOMBAT plasma source

The model was evaluated by comparisons to measurements of rf magnetic field structure and plasma properties in the Waves On Magnetized Beams and Turbulence (WOMBAT) helicon plasma source [16, 17]. The configuration of the WOMBAT used here consists of an upstream cylindrical plasma vessel driven by a double half-turn ($m = \pm 1$) antenna powered at 13.56 MHz. The 0.5 m long, 18 cm diameter quartz tube is within a solenoid providing an axial magnetic fields of 100 G and feeds into a downstream chamber 0.9 m in diameter and 2 m long. The downstream chamber is also surrounded by a solenoid and has an axial magnetic field of about 30 G. The antenna is 7 cm from the upstream end of the plasma source which is terminated with a metal plate. The diagnostics include a microwave interferometer to measure electron densities situated 5 cm from the downstream end of the quartz tube and rf magnetic field probes.

The WOMBAT geometry used in the model, shown in figure 1(*a*), is a close approximation of the experimental device for the upstream plasma zone. The downstream diffusion chamber has a smaller volume to reduce the computational burden. Parametrizations have shown that the reduced size of the downstream chamber has a measurable effect on plasma properties at the observation plane (indicated by the double arrows in figure 1(*a*)), but does not unduly prejudice the trends or conclusions discussed here. The static magnetic field structure, shown on the left side of figure 1(*a*), is essentially axial in the upstream plasma source with small radial oscillations which reflect the finite size of the solenoids. The reference point for cited magnitudes of the magnetic field, B_o, is indicated in figure 1(*a*). The base case conditions are Ar at 2 mTorr, 1250 W, 13.56 MHz and $B_\mathrm{o} = 100$ G. The Ar reaction mechanism is discussed in [25].

Predictions for the azimuthal (E_θ), axial (E_z) and radial (E_r) electric fields, power deposition, electron temperature and ion density are shown in figure 2 for the base case when excluding the electrostatic terms in the solution of Maxwell's equations. The peak ion density in the plasma source region is 3×10^{12} cm^{-3}, sustained by a peak electron temperature of 4.5 eV. Experimental microwave interferometry measurements provide an electron density of (4–5) $\times 10^{10}$ cm^{-3} at the reference point, compared to 7.5×10^{10} cm^{-3} from the model. The amplitudes of E_θ on opposites sides of the axis are essentially 180° out of phase reflecting the direction of the currents in the antenna segments. The amplitudes are zero on the axis due to the destructive interference of the waves launched by the opposing antennas having opposite phases. The axial wavelength in the far-field of the antenna is approximately 18 cm, which is well described by λ_{z2} of equation (1) which yields 20 cm. As the magnetic field is

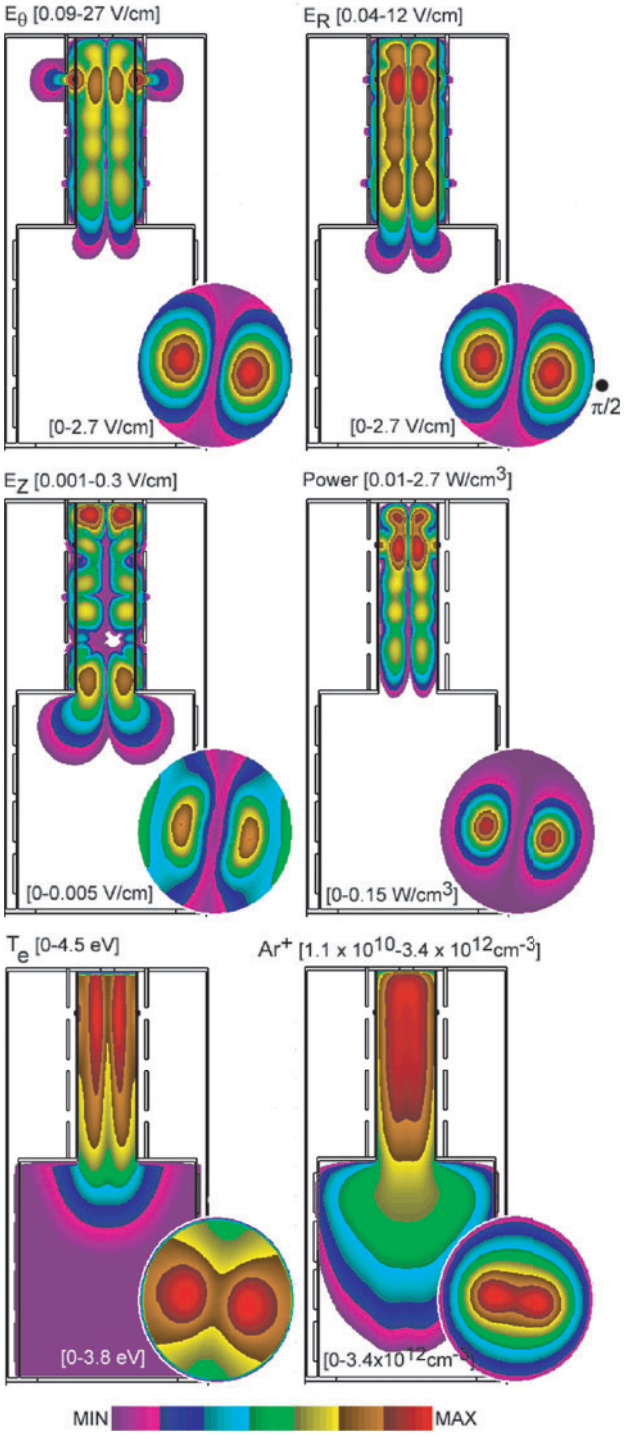

Figure 2. Plasma properties for the base case (Ar, 2 mTorr, 1250 W, $B_o = 100$ G): Amplitudes of E_θ, E_r, and E_z; power deposition, electron temperature and argon ion density. The background figures are (r, z) slices through the reactor at $\theta = \pi/2$ and $3\pi/2$. The foreground circular plots are (r, θ) slices at the reference plane shown in figure 1(a). The bracketed numbers above or to the left of each figure are the ranges of values plotted with the scale shown in the lower colour bar. With the exception of the electron temperature, the (r, z) slices are on a log-scale. The (r, θ) slices have a linear scale. The electric fields display W-mode like behaviour having an axial helicon wavelength of 18 cm. The dot shows the $\theta = \pi/2$ azimuth.

dominantly axial, the conductivity tensor dominantly couples the E_θ and E_r. As a result, in the far-field of the antenna, the amplitudes of these components are quite similar. In purely inductive coupling, E_z is only generated by those components of the tensor conductivity proportional to the B_r component of the static magnetic field (with azimuthal symmetry in the static magnetic field, $B_\theta = 0$). B_r is only significant between the solenoid segments and in the transition between the upper and lower chambers. As a consequence, E_z is largest at those locations, but with an amplitude which is always small compared to E_θ and E_r.

The electron temperature is maximum approximately at the half-radius where the electric field is maximum. T_e shows elongation downstream due to thermal conductivity along the magnetic field lines and the small cross-field mobility. T_e has significant azimuthal dependence for the same reason, peaking at an azimuth corresponding to the maximum in the electric field. This effect is likely overstated due to the collisional electron heating model. As a consequence, ionization sources also have significant azimuthal dependence, producing an ion density which has peaks at the same azimuths.

Although the electric field structure has key components which closely resemble that of the W-mode, we will at this juncture classify the base case as being in the H-mode. The key factor in this assignment is the behaviour of the phase of the electric field. The amplitudes of E_θ in the upper plasma zone at heights of approximately 62, 72, 83 and 93 cm at different phases during the rf cycle are shown in figure 3. (Although the amplitudes are positive and negative on opposite sides of the reactor, they are plotted as absolute values on a log scale to facilitate a larger dynamic range for viewing.) Amplitudes are shown for the first half cycle as those for the second cycle differ only in being opposite in symmetry. The travelling wave nature of E_θ along the axis is clear from the motion of the minimum in the amplitude (83 cm at $\phi = 0$, 72 cm at $\phi = \pi/4$ and 62 cm at $\phi = \pi/2$). E_θ has a complex modal structure at 93 cm in the vicinity of the antenna, but otherwise maintains an $m = |1|$ appearing pattern downstream. Note, however, that the field pattern does not appear to rotate in azimuth, maintaining fairly constant (r, θ) character downstream, differing only in amplitude as the wave is progressively damped. This has been experimentally seen as standing waves in $\hat{\theta}$ resulting from nearly equal amplitudes of the $m = +1$ and -1 components. The pattern does, however, rotate over a very narrow range of phases near $\phi = \pi/2$, shown at the bottom of figure 3, a consequence of the standing wave pattern in azimuth. This rotation propagates downstream with a phase delay. As discussed later, higher power cases have field amplitudes which continuously rotate during the entire phase. It is this lack of continuous azimuthal rotation which leads to the classification of the wave as being dominantly inductively coupled, or H-mode.

In experiments by Ellingboe and Boswell [16], a transition between H- and W-mode was observed upon increase in power between 1.1 and 1.6 kW. Their measurements were of the modal structure of the magnetic field. From these measurements, the modal structure of the electric field can be obtained. We attribute that transition to the onset of additional radial modes whose presence also correlates with azimuthal rotation of the amplitude of E_θ. For example, the amplitudes

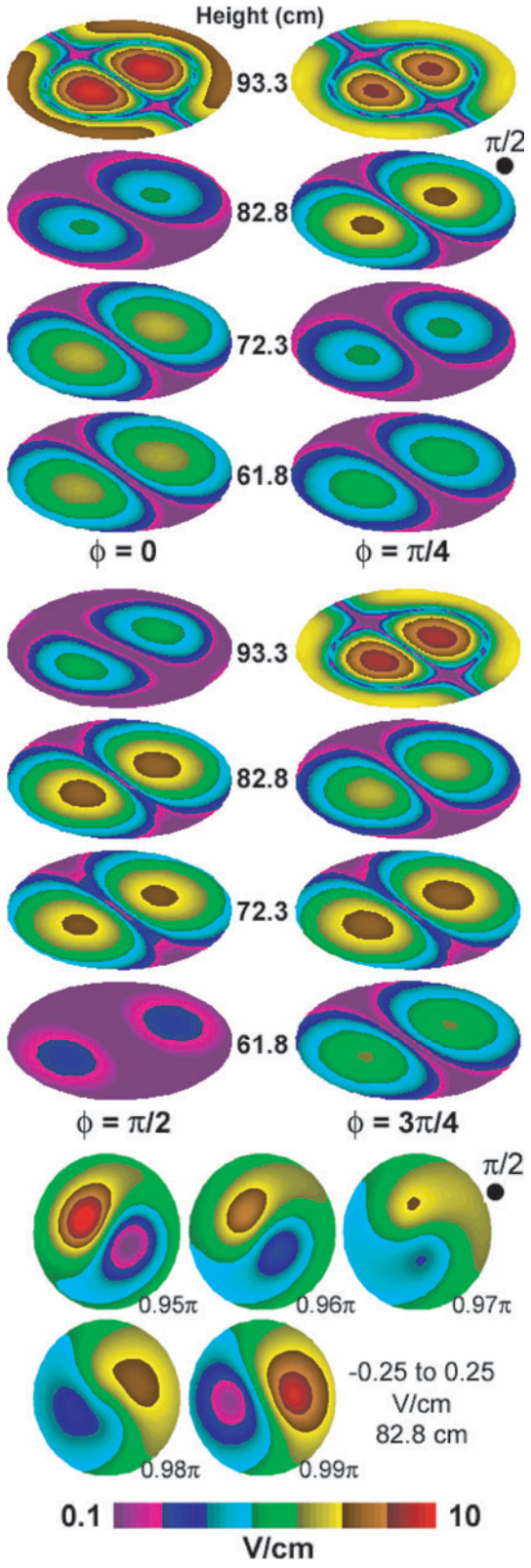

Figure 3. Absolute values of the E_θ (log scale) at different heights in the reactor at rf phases of 0, $\pi/4$, $\pi/2$ and $3\pi/4$. E_θ (linear scale) at a height of 83 cm for a finer resolution in phase approaching π is shown at the bottom. Plasma conditions are for the base case (Ar, 2 mTorr, 1250 W, $B_o = 100$ G). The dot shows the $\theta = \pi/2$ azimuth. Little rotation in electric field occurs except near $\phi = \pi$.

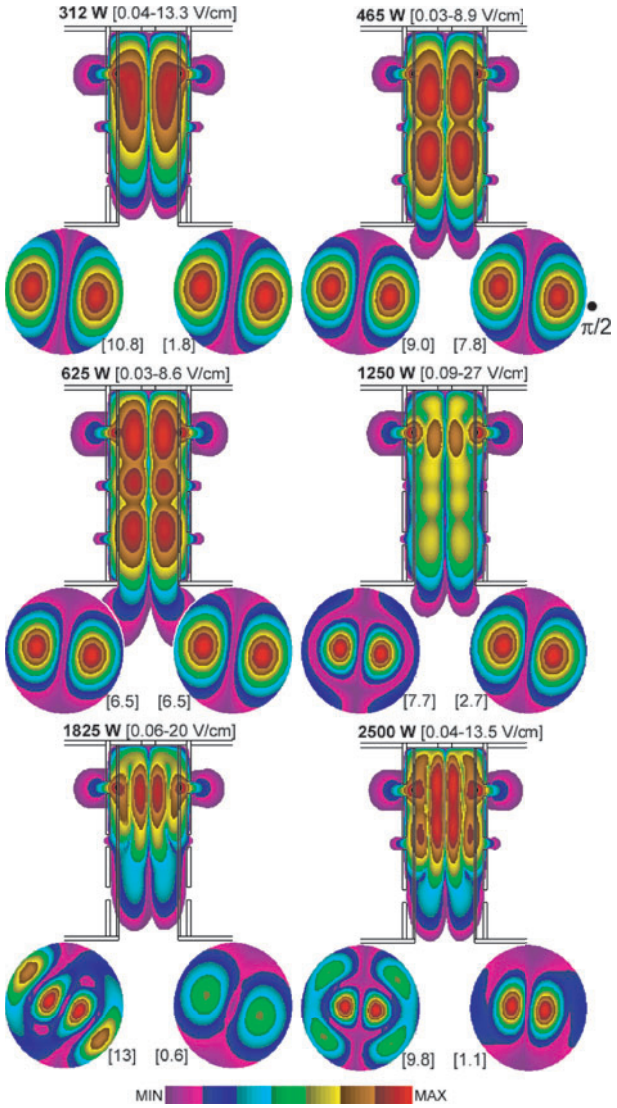

Figure 4. Amplitudes of E_θ for varying power deposition for otherwise the base case conditions (Ar, 2 mTorr, $B_o = 100$ G). The left (r, θ) slice is at a height a 4–5 cm below the antenna. The right (r, θ) slice is at the reference height. The labelling scheme is the same as for figure 2 with the (r, z) slices having log scales and the (r, θ) having linear scales with zero minimum value. The dot shows the $\theta = \pi/2$ azimuth. A transition occurs between 1250 and 1825 W in which higher order radial modes are produced.

of E_θ are shown in figure 4 for powers of 312 to 2500 W. The amplitudes are shown only in the upstream plasma source with two (r, θ) slices at heights near the transition to the lower chamber and near the antenna. At 312 W, the electron density (peak value 1.1×10^{12}, 3×10^{10} cm^{-3} at the reference point) is sufficiently low and the resulting helicon wavelength sufficiently long (36 cm) ensuring that multiple wavelengths are not contained within the source region. Increasing power to 465 and 625 W increases the peak electron density to 1.6×10^{12} and 1.9×10^{12} cm^{-3}, resulting in wavelength shortening (30 and 26 cm) and producing travelling waves within the source region. By increasing power to 1250 W (base case), the wavelength shortens sufficiently, and radial modal patterns begin to develop near the antenna, but, as discussed above, the character of the wave is still H-mode.

On increase in power deposition to 1825 W (peak electron density 4.2×10^{12}, 9×10^{10} cm^{-3} at the reference point), there is a change in mode structure, predominantly in the radial direction near the antenna with an apparent lengthening of wavelength in the axial direction. Further increase in power to 2500 W (peak electron density 5.5×10^{12}, 1.3×10^{11} cm^{-3} at the reference point) produces additional azimuthal mode structure, while decreasing the axial wavelength commensurate with the increase in electron density.

Components of the electric field, power deposition, electron temperature and ion density for the 1825 W case are shown in figure 5. The amplitude of E_θ at 1825 W is shown in figure 6 at the same heights and phases as in figure 3 for the 1250 W case. Although downstream the modal structure of E_θ resembles that of the H-mode cases, the structure in the near field of the antenna has higher order radial and azimuthal modes, which agrees with experimental observations for a transition to the W-mode [16]. The helicity provided by these modes results in a rotation of the electric field in the entire length of the plasma zone, providing credence for the classification of the 1825 W cases as being W-mode. Note that the decrease in the axial wavelength for the 1825 W case results in a more highly confined power deposition in the source region, and, compared to the H-mode case, a more centrally peaked electron temperature and ion density. A finer scan in power deposition showed that at 1500 W there is mixed H- and W-mode character, signifying that perhaps 1500 W is the transition point between the two modes, an assignment that may depend on the inclusion of electrostatic terms.

Experimental concurrence with these observations are as follows. The dynamics of the axial wavelength appears to be captured. The experimental observation is that upon crossing into the W-mode with increasing power, the axial wavelength increases and then decreases with further increase in power [17]. The approximate power at which the H- to W-mode transition occurs is also reproduced, approximately 1500 W [16]. The shift in plasma density towards the axis upon transitioning to the W-mode is captured as well [26]. Given that our assignment for transition to the W-mode is correct, we do not capture the rapid increase in plasma density at the reference plane with increasing power as measured in experiments at the W-mode transition. If we accept the proposition [16, 17, 24] that transit time wave–particle heating is significant, the model would be expected to miss this increase in plasma density just downstream of the antenna. For example, the ion density (equal to electron density) obtained from microwave interferometry and the model for the reference point are shown in figure 7(*a*). The experimental values were multiplied by 1.5. The computed slope for increasing plasma density with power agrees well with the experimental slope below 1500 W. At powers above the W-mode transition, the model does predict a steeper slope, however, the slope is less than that obtained by the experiment. We attribute this difference to limitations of our collisional power deposition model and the lack of long mean free path transport which produces higher rates of ionization. This disagreement is likely also as a consequence of the lack of the TG mode in these calculations, and may indicate the importance of the TG mode in experimentally observed jumps in plasma density when increasing power.

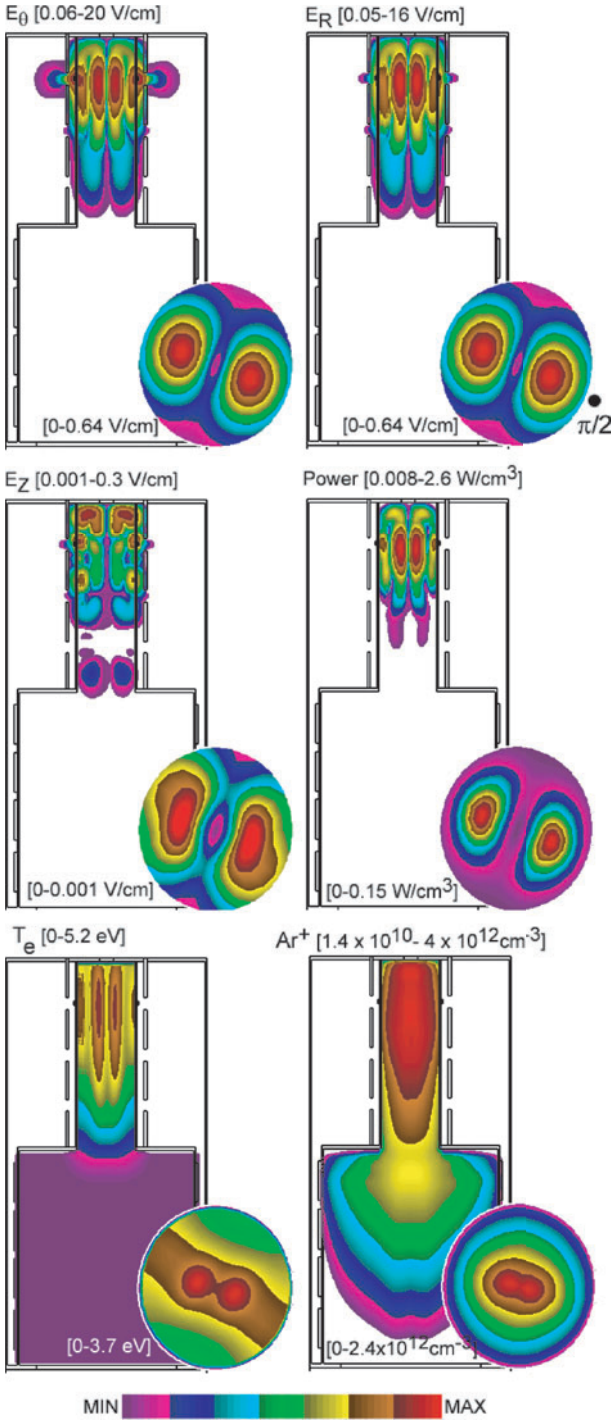

Figure 5. Plasma properties for 1825 W but otherwise the base case conditions (Ar, 2 mTorr, $B_o = 100$ G): amplitudes of E_θ, E_r and E_z; power deposition, electron temperature and argon ion density. The labelling scheme is the same as in figure 2. The dot shows the $\theta = \pi/2$ azimuth. The electric field and power deposition are dominated by radial modal structure, which produces more near-axis ionization.

The experimental trends in antenna current appear to be less well captured or may be indicative of a less than clear assignment of the transition to the W-mode. In the experiments, the antenna current and voltage increases upon transition into the W-mode. Predicted antenna currents as a

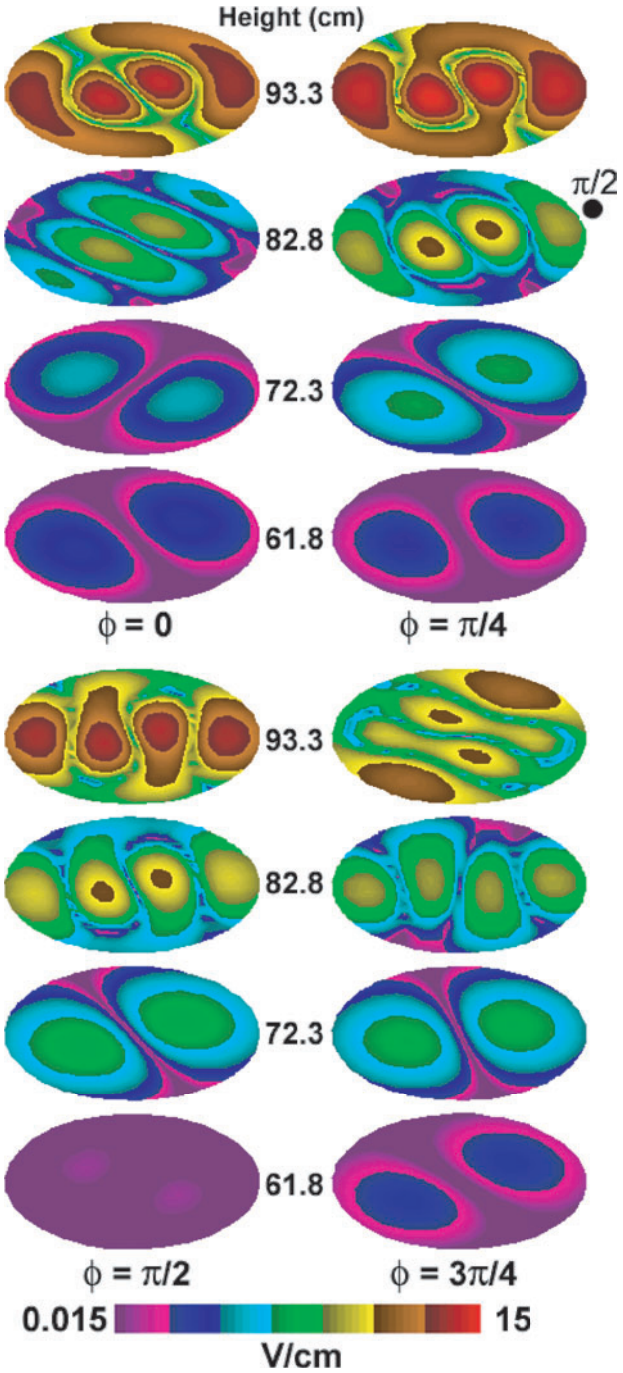

Figure 6. Absolute values of the E_θ (log scale) at different heights in the reactor at rf phases of 0, $\pi/4$, $\pi/2$ and $3\pi/4$. Plasma conditions are for a power deposition of 1825 W but otherwise the base case conditions (Ar, 2 mTorr, $B_o = 100$ G). The dot shows the $\theta = \pi/2$ azimuth. There is continuous rotation of the electric field at all heights in the source region.

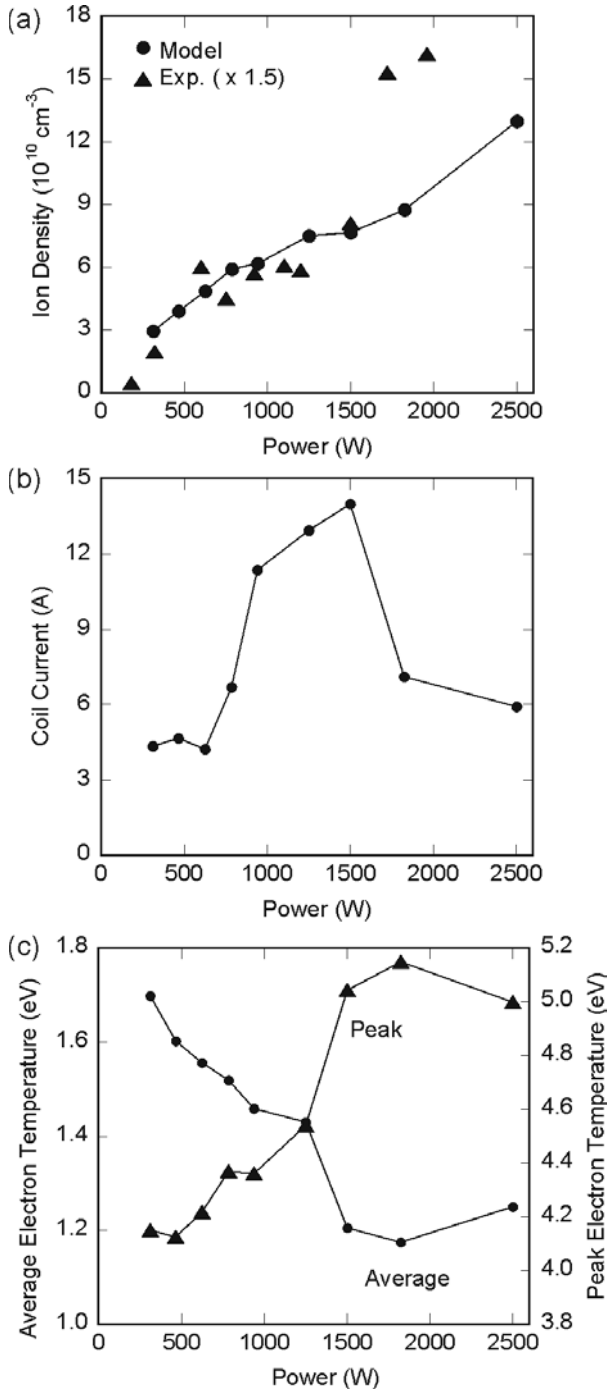

Figure 7. Plasma properties as a function of power for otherwise the base case conditions (Ar, 2 mTorr, $B_o = 100$ G). (*a*) Ion density (equal to the electron density) at the reference height from the model and measured experimentally using microwave interferometry. The experimental values are multiplied by 1.5. The increase in ion density in the W-mode is less dramatic in the calculations. (*b*) Antenna current. (*c*) Peak and average electron temperature in the upstream plasma source.

function of power deposition are shown in figure 7(*b*). We do capture an abrupt increase in antenna current at approximately 1 kW which correlates with the formation of radial models, and, on that basis, might be an indication of the onset of the W-mode, though the magnitude of the predicted current is about one-third to one-half that experimentally observed [16]. Our formal assignment was made on the basis of the rotation of the electric field, which we find occurs at powers of about 1500 W. We also observe systematic trends in the electron temperature as shown in figure 7(*c*). The computed peak electron temperature increases monotonically with increasing power until the W-mode transition, at which time T_e saturates. This may indicate the onset of a more efficient ionization

process. While the peak T_e increases, the average T_e in the source region actually decreases until the W-mode transition, at which time it also saturates. This indicates that larger gradients and more peaked electron temperatures occur with increasing power.

4. Characteristics of MEICPs: an industrial reactor

With these baseline observations provided by the well characterized WOMBAT source, we then investigated the dynamics of a more industrially relevant reactor. The reactor geometry and magnetic field configuration for this investigation are shown in figure 1(*b*) and are based on the Trikon Mori plasma source [27, 28]. The top of the reactor consists of a quartz bell-jar surrounded by a solenoid which produces a flaring magnetic field into the lower chamber. (The actual Trikon Mori source has a more extended lower chamber than shown in figure 1(*b*) which allows for more diffusive transport and ultimately more uniform fluxes to the substrate than shown here.) Magnitudes of the magnetic field refer to an on-axis point shown in figure 1(*b*) as B_o. An $m = 1$, Boswell type antenna [29] is fitted on the exterior of the bell jar and consists of two saddle coils approximately 90° in extent and 90° in separation. The (r, z) slices taken through the three-dimensional figures of plasma are for azimuths in the middle of one of the half-cylinders of the antenna (right face, $\theta = \pi/2$) and through the gap between the half-shells of the antennas (left face, $\theta = 0$). The double-arrows in figure 1(*b*) show the axial location where plasma properties in (r, θ) planes are displayed.

The base case conditions are for an Ar gas pressure of 10 mTorr, power deposition of 800 W, magnetic field (at the reference point) of 125 G and antenna frequency of 10 MHz. As a point of departure, the three components of the electric field are shown in figure 8 for the base-case conditions. Power deposition, electron temperature ion source and Ar^+ ion density are shown in figure 9. In the absence of the magnetic field, E_θ would, at best, penetrate a classical skin depth which, for these conditions, is a few centimetres. The low cross field mobility allows penetration of B_r and B_z into the volume of the plasma, which in turn produces E_θ. The maxima in the E_z and E_θ components occur about the axial and azimuthal antenna segments. E_r, being generated purely by plasma currents, is maximum in the bulk plasma at a half radius. Due to the mirror symmetry of the antennas, electric fields are zero on axis.

Power deposition is dominated by the axial electric fields at the periphery of the plasma in the bell jar, and by the radial and azimuthal components of the electric field in the volume of the plasma in the downstream region, indicating there being mixed H- and W-modes. As electrons are well magnetized at these static magnetic fields, the electron temperature is azimuthally non-uniform and mirrors regions of largest power deposition. Hot electrons (4–5 eV) diffuse downstream on the fields lines. The resulting sources of ionization and Ar^+ density are heavily influenced by the non-uniform electron temperature, producing lobes of ionization which are maximum near the antenna segments (H-mode) and in the bulk plasma downstream (W-mode). The ions, being less magnetized than the electrons, mitigate these non-uniform

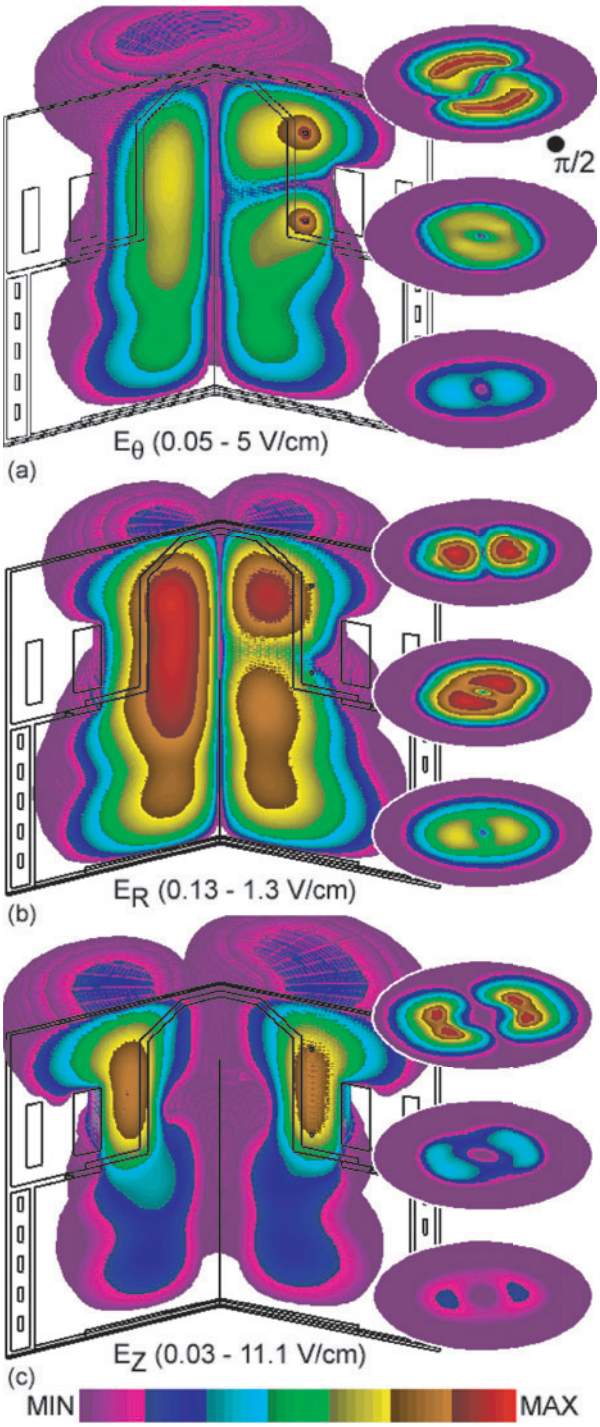

Figure 8. Amplitudes of electric fields in the industrial reactor. (*a*) E_θ, (*b*) E_r and (*c*) E_z. The conditions are for the base case (Ar, 10 mTorr, $B_o = 125$ G, 800 W, 10 MHz). The (r, z) slices are at azimuths that pass through the antenna (right face, $\theta = \pi/2$) and between the antennas (left face, $\theta = 0$). The (r, θ) slices are at the heights indicated in figure 1(*b*). The values are plotted on a log-scale with a range indicated below each figure. The dot shows the $\theta = \pi/2$ azimuth. Note the rotation in electric field with propagation downstream.

sources through cross field diffusion. The (r, θ) distribution of ion density, peaking at 3×10^{12} cm^{-3}, is highly non-uniform in the bell jar where the static magnetic fields are largest and ion sources most asymmetric. Near the substrate, where the

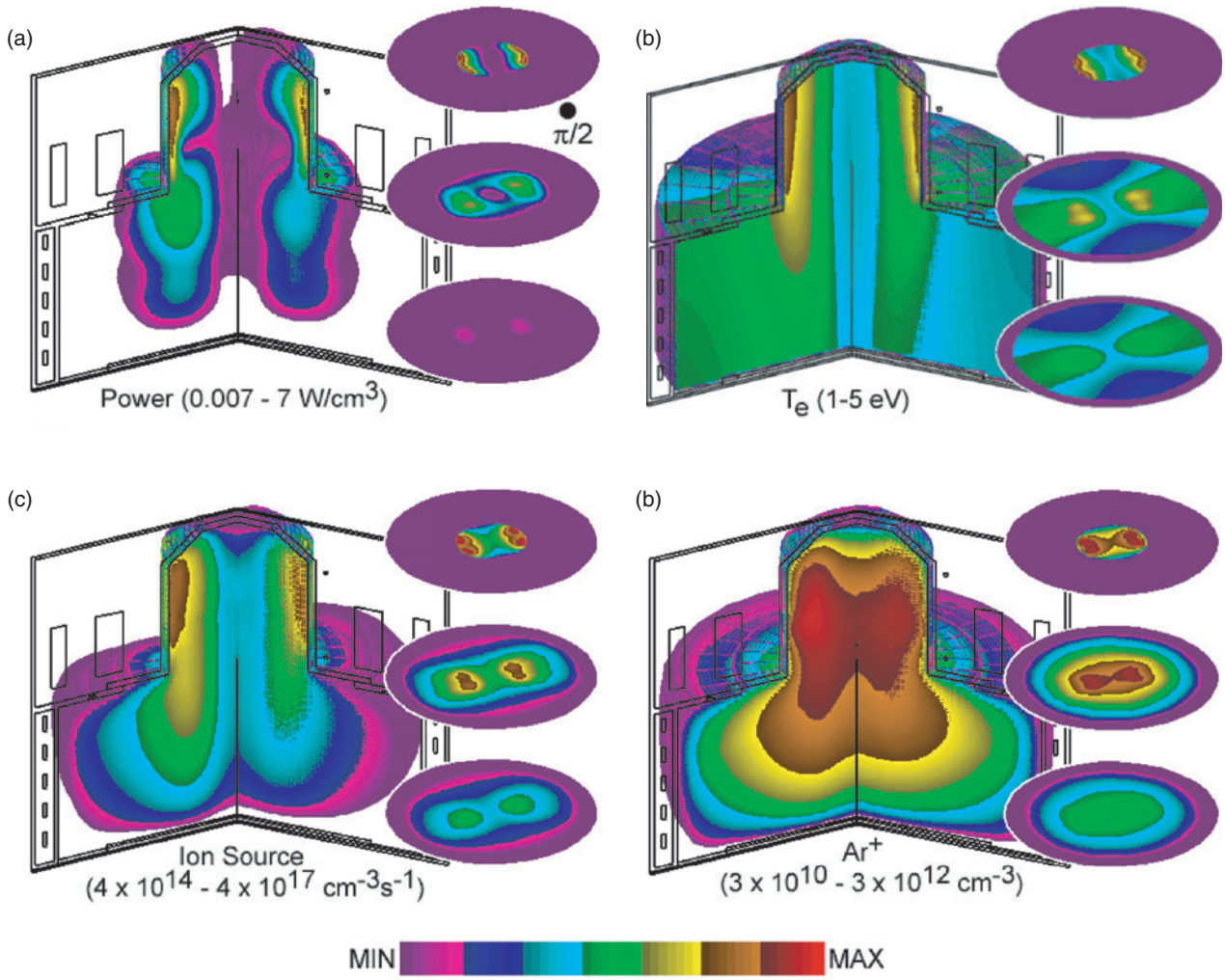

Figure 9. Plasma properties for base case (Ar, 10 mTorr, $B_o = 125$ G, 800 W, 10 MHz). (*a*) Power deposition, (*b*) electron temperature, (*c*) ionization source and (*d*) ion density. The labelling scheme is the same as for figure 8. The dot shows the $\theta = \pi/2$ azimuth. With the exception of the electron temperature, values are plotted using a log scale. Power deposition resembles H-mode in the bell jar producing non-uniform ionization which is mitigated downstream by cross-field diffusion.

magnetic field is flaring and of lower magnitude, the uniformity of the ion density significantly improves.

This antenna should, under idealized conditions (cylindrical plasma of constant radius, constant axial magnetic field) support an $m = 1$ electromagnetic field. In industrial reactors where magnetic fields are rarely uniform and reactors have non-cylindrical features, the electromagnetic structure is often multi-modal. Nevertheless, evidence of $m = 1$ behaviour can be seen in the phase and time dependence of the phase and amplitude of the azimuthal component of the electric field shown in figure 8. The amplitude of the azimuthal component electric field is shown in figure 10 at different phases during the rf cycle in the (r, θ) plane at $z = 15$ cm. Note the rotation of the E_r and E_θ electric fields as they propagate downstream a signature, perhaps, of a helicon-like mode. The electric field amplitude rotates clockwise in a cork-screw pattern as one moves up the axis of the reactor. The spatial dependence is strikingly similar to that for a pure $m = 1$ mode in spite of the non-idealized conditions. Although not shown here, the clockwise orientation of the rotation reverses as the antenna is traversed from bottom to top. This rotation occurs, on a W cm^{-3} basis, at lower powers than in the WOMBAT source. This trend may be attributable to the flaring magnetic field, and the antenna which contains axial segments, which produce all three components of the electric field having approximately the same amplitudes. Although the magnetic field in the bell jar is 125 G, in the centre of the downstream chamber the magnetic field is only 45 G, producing a smaller helicon wavelength and, perhaps, enabling the rotation at lower electron densities.

The axial wavelength of the helicon wave is proportional to the magnetic field, and inversely proportional to the rf and electron density (and hence power deposition). The variation of the helicon wavelength with these parameters, even in non-idealized geometries, is clearly reflected in the axial and radial mode structure of the electric field. For example, the azimuthal electric field for 2, 20 and 40 MHz are shown in figure 11 for conditions which are otherwise the same as the base case (compare with E_θ in figure 8(*a*) for 10 MHz). The resulting power deposition and ion density for 2 MHz and 40 MHz are shown in figure 12 (compare with figures 9(*a*) and (*d*) for 10 MHz). At 125 G peak field, the mid-reactor plasma densities for these cases are (1.5–2) $\times 10^{12}$ cm^{-3}, producing

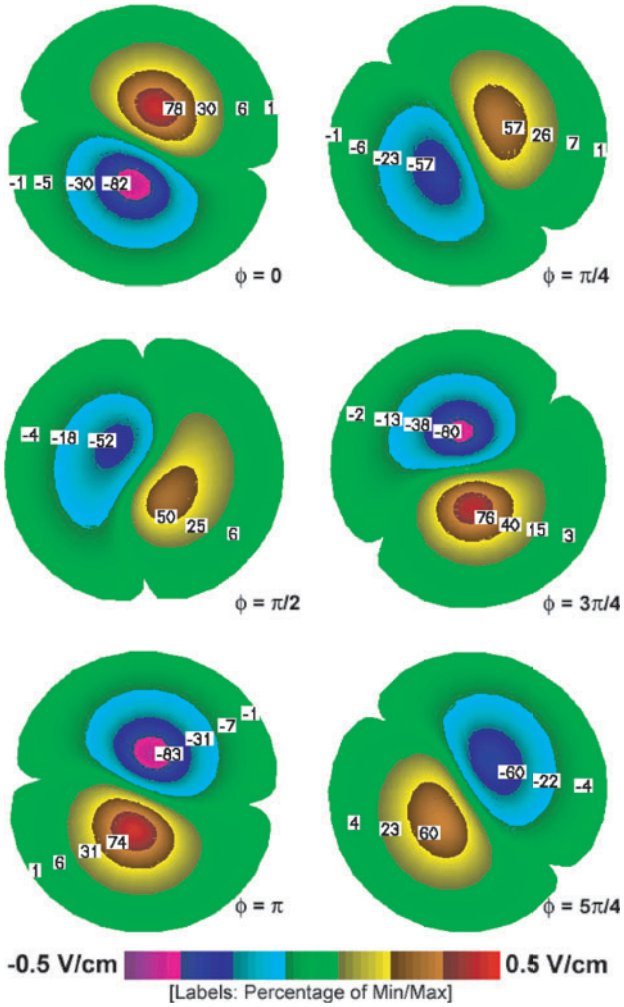

Figure 10. Azimuthal electric field E_θ at a height of 15 cm as a function of phase during the rf cycle for the base case (Ar, 10 mTorr, $B_o = 125$ G, 800 W). The labels are the per cent of the minimum/maximum electric field, 0.5 V cm^{-1}. Rotation of the electric field occurs continuously during the rf cycle.

high density limit axial helicon wavelengths of 31 cm at 2 MHz decreasing to 7 cm at 40 MHz. This span of wavelengths ranges from near field at 2 MHz (long wavelength) to far-field 40 MHz (short wavelength). Given that the radius of the bell jar is 8 cm and height of the reactor 30 cm, the helicon wavelength at 2 MHz is too long to enable a higher order, or in principle, for fundamental modes to form. There is little propagation downstream. The coupling should be limited to H-mode. In all characteristics, the 2 MHz case resembles H-mode coupling with the exception of rotation of the electric field. E_θ has a similar rapid rotation near phase $\phi = \pi$ as in the WOMBAT H-mode cases, but has a somewhat more continuous rotation downstream. Since in the centre of the downstream chamber the magnetic field drops to 45 G, the helicon wavelength is reduced approximately one-third, thereby enabling rotation.

At 40 MHz, the decrease in the wavelength is reflected in the shorter skin depth, a change in the radial mode structure and in axial propagation. The far-field propagation enables interference, higher order modes and a continuous rotation of E_θ as shown in figure 13 for a height of 15 cm. Note also that the short wavelength and higher order mode structure

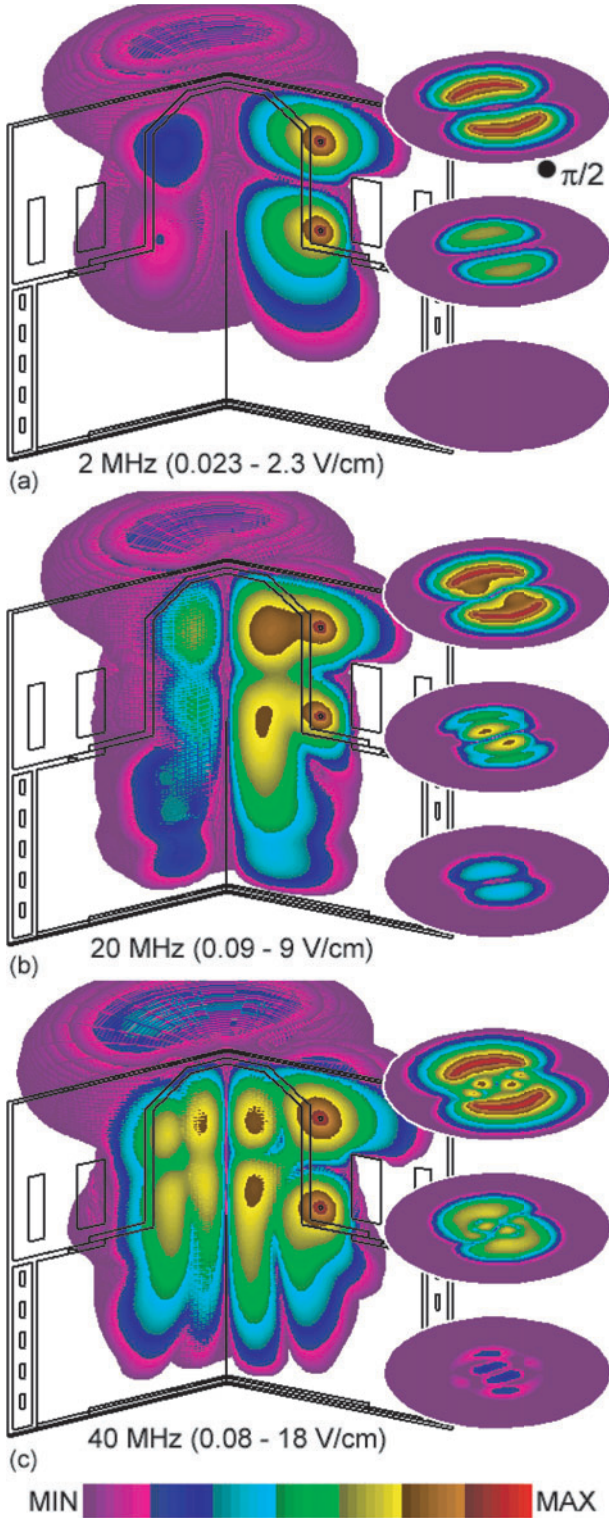

Figure 11. Amplitudes of the azimuthal electric field E_θ for different frequencies for plasma conditions that are otherwise the same as the base case (Ar, 10 mTorr, $B_o = 125$ G, 800 W). (*a*) 2 MHz, (*b*) 20 MHz and (*c*) 40 MHz (see figure 8 for the 10 MHz case). The labelling scheme is the same as for figure 8. The dot shows the $\theta = \pi/2$ azimuth. At 2 MHz, the electric field resembles H-mode in the bell jar. At 40 MHz, complex radial modes are produced.

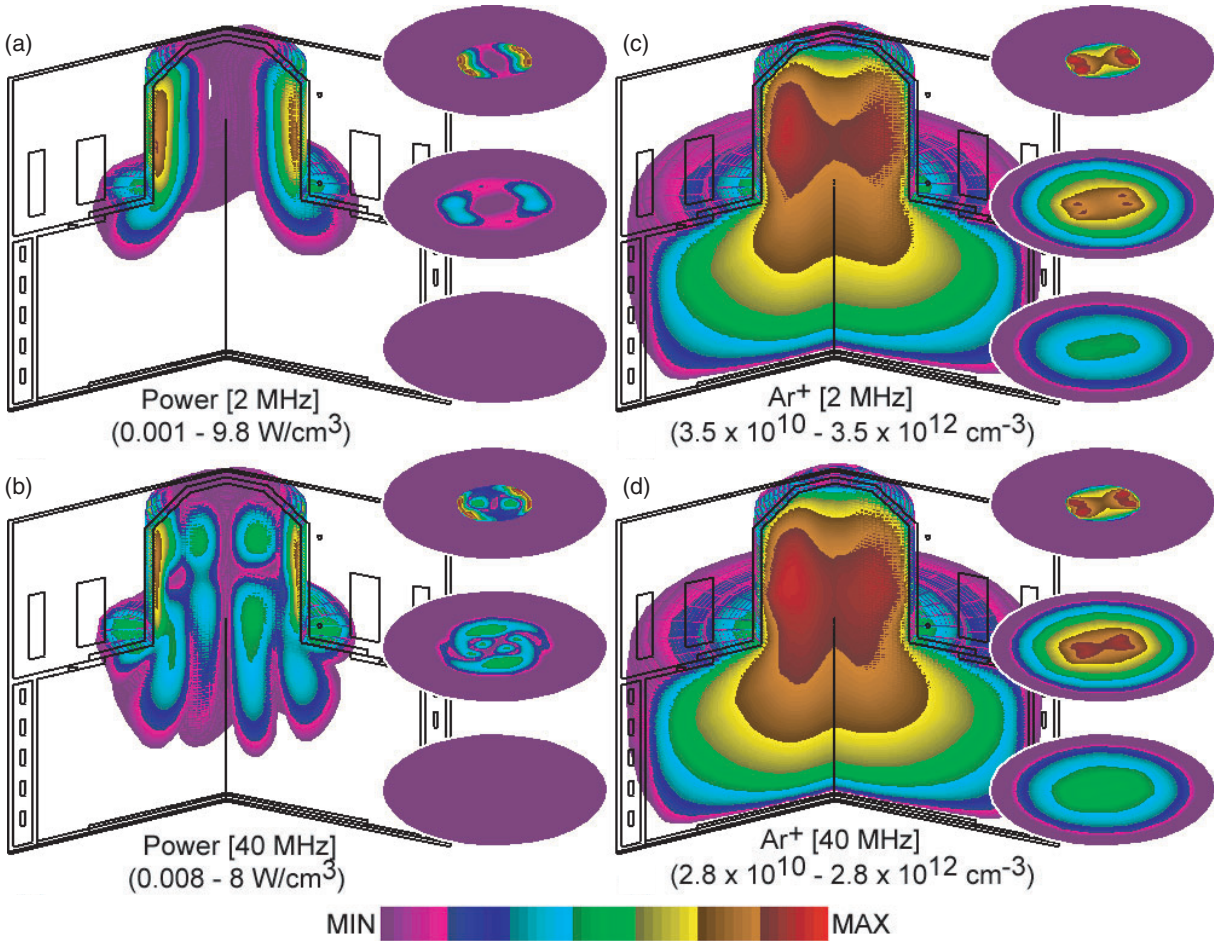

Figure 12. Plasma properties for frequencies of 2 and 40 MHz for plasma conditions that are otherwise the same as the base case (Ar, 10 mTorr, $B_o = 125$ G, 800 W). (*a*) Power deposition at 2 MHz, (*b*) ion density at 2 MHz, (*c*) power deposition at 40 MHz and (*d*) ion density at 40 MHz (see figure 9 for the 10 MHz case). The labelling scheme is the same as for figure 8. Power deposition is closer to the axis at 40 MHz where radial modes dominate.

produces power deposition in the interior of the bell jar and ultimately a more uniform ion density in the vicinity of the substrate. Although the modal structure at 40 MHz is mixed, the signatures (rotation of electric field and volumetric power deposition) motivate assigning W-mode to this case, whereas the 2 MHz case is likely a H-mode and at best a mixed H-mode and W-mode.

The amplitude of E_θ and the density of Ar^+ at the substrate for 800 W are shown in figure 14 for B_o of 20, 125 and 250 G. As B_o increases from 20 to 125 G, the helicon wavelength increases from 5.5 to 20 cm. The shorter wavelength at 20 G results in radial modes and produces power deposition and ionization sources closer to the axis. This ultimately results in a fairly uniform ion flux to the substrate. Although there are distinct radial modes, for all practical purposes E_θ does not rotate, and so classification as a W-mode is problematic. At B_o = 250 G, λ_{z2} is too large to allow radial modes to form in the bell jar as the wave is cut-off. Radial modes do appear to form downstream where the magnetic field is smaller, suggesting a H-mode-like behaviour in the bell jar and W-mode-like behaviour downstream. These assignments are reinforced by the rotation of E_θ. In the bell jar, E_θ rotates only between phases of 0.75π and 1.25π indicating a standing wave in $\hat{\theta}$, whereas downstream rotation is fairly continuous during the rf cycle. This behaviour may reflect what fraction of the amplitude exists in the $m = -1$ wave; a large fraction in the source region and a low fraction in the diffusion region. The end result is more near axis power deposition, and again, a fairly uniform ion flux. The ion flux is least uniform at $B_o = 125$ G where $\lambda_{z2} = 14$ cm and power deposition is furthest from the axis.

Similar trends occur when varying power. E_θ and the density of Ar^+ at the substrate for $B_o = 125$ are shown in figure 15 for 300 and 1500 W. As the electron density scales with power deposition, lower power deposition corresponds to longer helicon wavelengths. As such, E_θ has little, if any, radial structure at 300 W upstream with negligible on-axis power deposition and little rotation of E_θ. Downstream, there is nearly continuous rotation of E_θ, though no higher order radial mode and little power is deposited. The end result is a non-uniform ion flux at the substrate and an assignment of at best mixed H- and W-modes. At 1500 W, λ_{z2} shortens sufficiently so that radial modes are formed, producing near axis power deposition which is more localized in the bell jar. There is moderate rotation of E_θ both in the bell jar and downstream. These conditions produce W-mode behaviour.

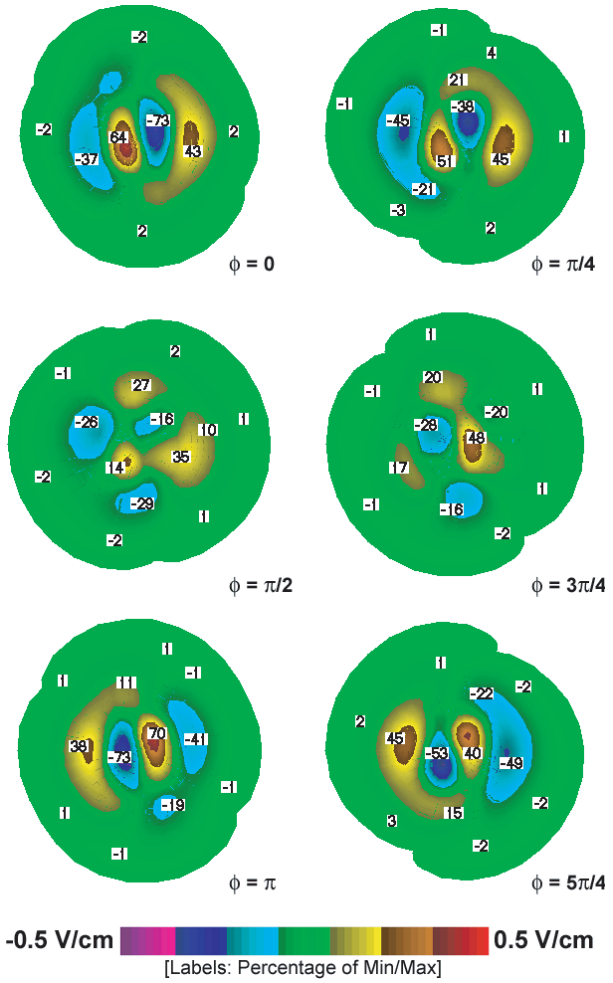

Figure 13. Azimuthal electric field E_θ at a height of 15 cm as a function of phase during the rf cycle for 40 MHz but otherwise the base case conditions (Ar, 10 mTorr, $B_o = 125$ G, 800 W). The labels are the per cent of the minimum/maximum electric field, 0.5 V cm^{-1}. Rotation of the electric field occurs continuously during the rf cycle with complex radial mode structure.

5. Mode structure with electrostatic coupling

The consequences of electrostatic coupling producing slow waves (TG mode) in helicon sources has been discussed in many previous works [7–14, 30–34]. In general, electrostatic coupling is thought to increase the power absorption in the periphery of the plasma [5, 16, 30, 31] and shorten the helicon damping length [8, 33]. Although a complete systematic investigation of these effects is beyond the scope of this study, some of these trends can be observed from the three-dimensional model when including the electrostatic term in Maxwell's equations. To this end, the WOMBAT geometry was modelled when including the electrostatic terms and results are shown here for a power deposition of 1500 W. Similar results were obtained for other powers. In the absence of electrostatic coupling, based on an examination of the mode structure of the electromagnetic waves (e.g. lack of rotation of E_θ), a power of 1500 W would be classified as being at the threshold of the E–W transition. Power deposition and the radial electric field, E_r, are shown without and with electrostatic coupling in figure 16 for 1500 W. E_θ at

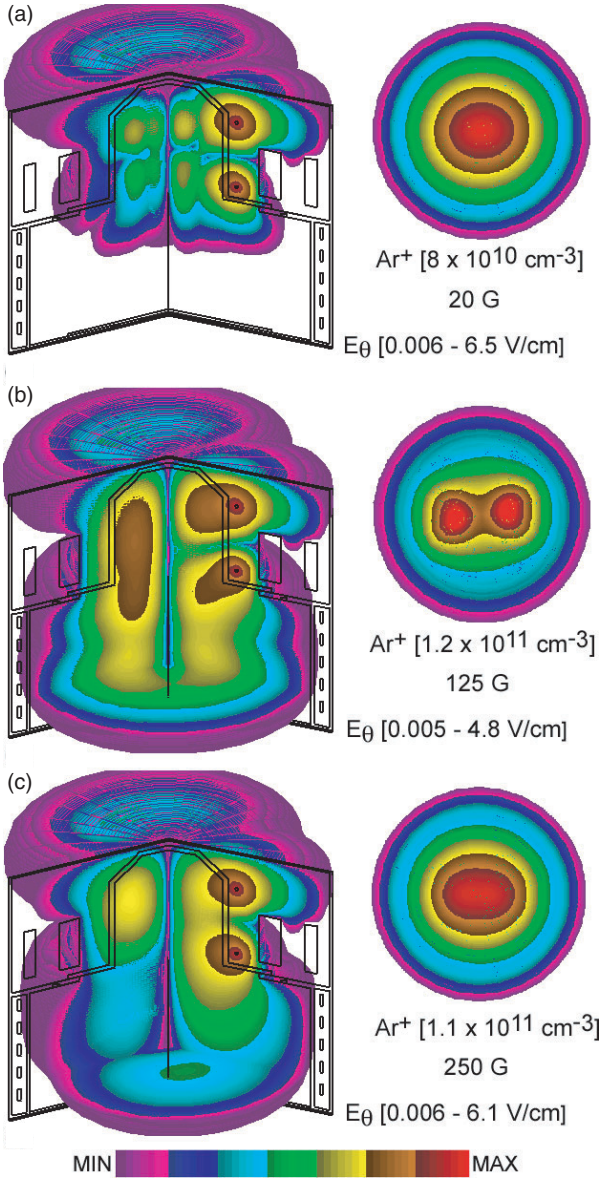

Figure 14. Amplitudes of the azimuthal electric field E_θ and ion density at few centimetres above the substrate for different static magnetic fields for plasma conditions that are otherwise the same as the base case (Ar, 10 mTorr, 10 MHz, 800 W). (*a*) 20 G, (*b*) 125 G and (*c*) 250 MHz. The labelling scheme is the same as for figure 8. More uniform ion fluxes are obtained at 20 and 250 G.

different heights in the reactor are shown in figure 17 for these cases.

The cited effects attributed to the slow wave are evident in these results when including the electrostatic terms. When keeping the total power deposition constant, power is redistributed to the periphery of the reactor in the vicinity of the antenna, as shown in figure 16(*a*). The axial extent of the power deposition by the helicon mode is also shortened. Examination of the components of the electric field shows that the radial distribution of E_r is most affected in this geometry by the inclusion of the electrostatic fields, as shown in figure 16(*b*). The regions in which the power deposition in the periphery of the reactor increases also correspond to those where E_r is most enhanced.

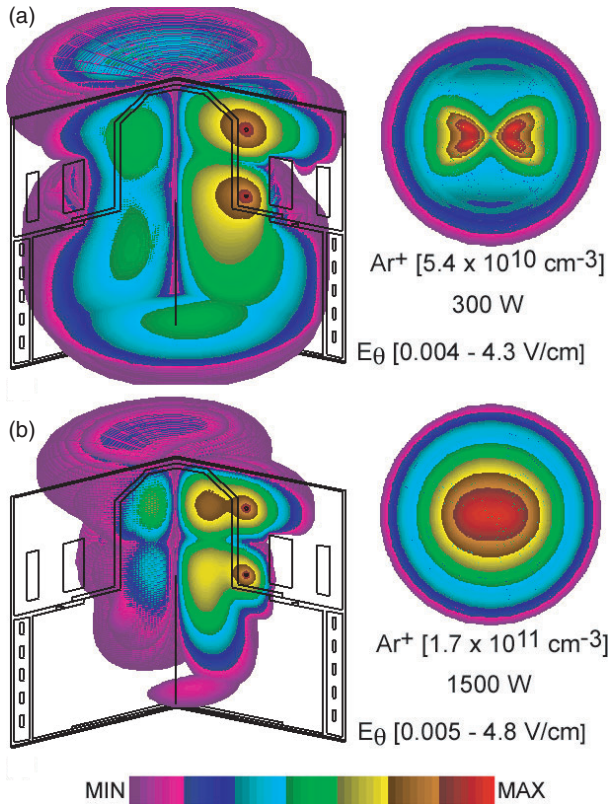

Figure 15. Amplitudes of the azimuthal electric field E_θ and ion density at few centimetres above the substrate for different power deposition for plasma conditions that are otherwise the same as the base case (Ar, 10 mTorr, 10 MHz, $B_o = 125$ G). (*a*) 300 and (*b*) 1500 W (see figures 8 and 9 for the 800 W case). The labelling scheme is the same as for figure 8. More uniform ion fluxes are obtained at 1500 W due to there being more power deposition near the axis and higher in the reactor.

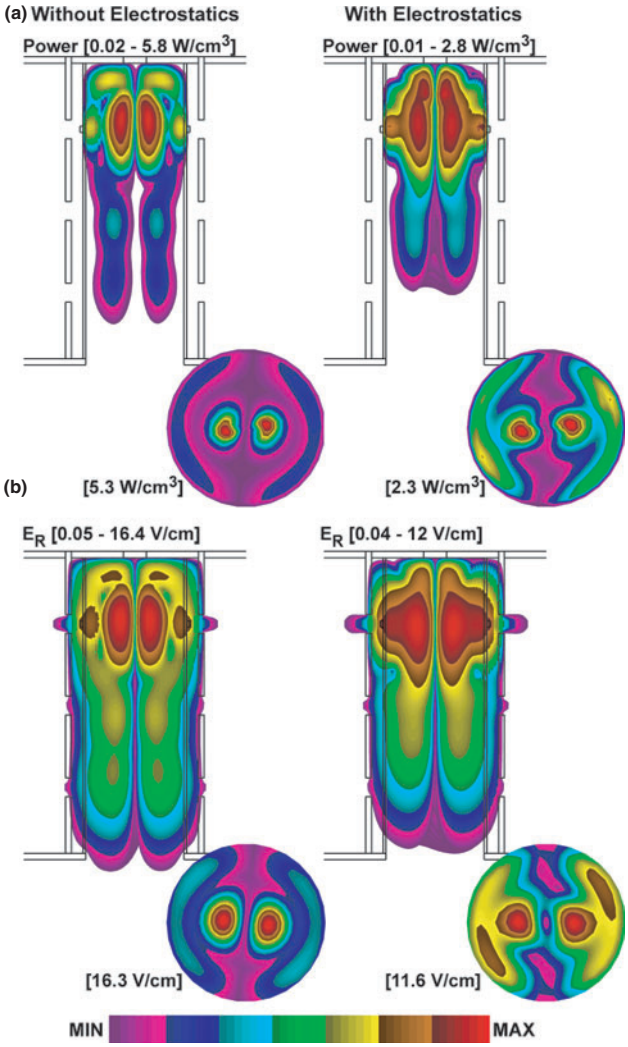

Figure 16. Plasma properties for the WOMBAT geometry (Ar, 2 mTorr, $B_o = 100$ G) for 1500 W when excluding and including the electrostatic terms in Maxwell's equations. (*a*) Power deposition and (*b*) amplitude of E_r. The labelling scheme is the same as in figure 2. The $r\theta$ slice is for a height of 98 cm near the antenna. When including the electrostatic terms, more power deposition is distributed to the periphery of the reactor and is attributed to E_r.

In the absence of electrostatic coupling, this case is just at the threshold of the E–W transition. There is clear axial propagation of helicon like waves, however, as shown in figure 17(*a*), there is no rotation in E_θ and radial modes have yet to form. When including the electrostatic terms, E_θ rotates as it propagates downstream and radial modes begin to form near the antenna. Since the helicon mode is damped more rapidly with the electrostatic terms, the magnitude of E_θ is diminished downstream. When including the electrostatic terms, the E–W transition has clearly been made. The mechanism for triggering the E–W transition at a lower power deposition with the electrostatic terms is likely subtle, such as a redistribution of plasma density.

We note that the computational technique used to include the electrostatic terms is based on a perturbation approximation for the charge density [20]. As such, an artificially high damping term may have been used to assure that the charge density was sufficiently small for the perturbation approach to be valid. In this regard, the effects shown here for including electrostatics is likely a lower estimate.

6. Concluding remarks

Characteristics of H- to W-mode transitions in MEICPs have been investigated using results from a three-dimensional plasma equipment model. When excluding electrostatic terms in the solution of Maxwell's equations, experimental observations for mode structure and transitions from H- to W-mode have been reproduced for an $m = 1$ plasma source in a uniform magnetic field. The transition from H- to W-modes occurs coincident with the formation of J_1-Bessel function structure in E_θ, onset of rotation of the electric fields and increase in antenna current. Plasma sources may have helicon-like waves (at least as characterized by wavelength) but operate in dominantly an H-mode. A reasonable scaling parameter to determine whether W-modes may occur is $\lambda_{z2}/d \leqslant 1$ where d is the transverse dimension of the plasma source. Many cases were encounter were where $\lambda_{z2}/L \leqslant 1$ (L is the longitudinal dimension) and H-mode behaviour was observed. Plasma characteristics of an industrial MEICP source having a flaring magnetic field and a Boswell antenna were also investigated. Similar scaling laws were observed as for the dominantly solenoidal plasma source. Simultaneous H- and

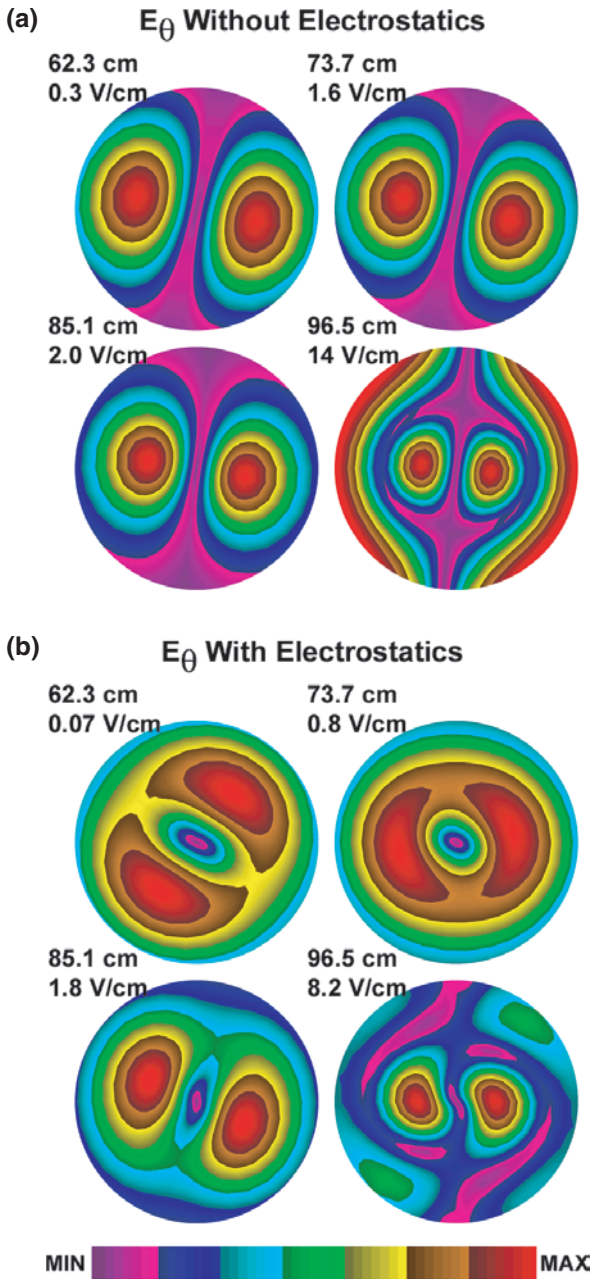

Figure 17. E_θ at different heights in the reactor when (*a*) excluding and (*b*) including electrostatic terms in solution of Maxwell's equations for the WOMBAT geometry (Ar, 2 mTorr, $B_o = 100$ G, 1500 W). All plots are separately normalized on linear scales with the maximum value noted. Without the electrostatic terms, the plasma is just at the H- to W-mode transition. With the electrostatic terms, the transition has occurred.

W-mode behaviour occurred (as characterized by radial modes and rotation of the electric field) in different regions of the plasma source depending on the local values of $\lambda_{z2}/d \leqslant 1$ and $\lambda_{z2}/L \leqslant 1$. When including electrostatic terms in solution of Maxell's equations, cited experimental observations were reproduced. When keeping the power deposition constant, more power was proportionally distributed to the periphery of the reactor and the helicon damping length was shortened. We also noted that the H- to W-mode transition occurred at lower power, an effect likely a result of a redistribution of plasma density. Although the model employed in this study lacked a kinetic description of power deposition in solution of Maxell's equations, a condition which likely overemphasized plasma non-uniformities in density and temperature, a wide range of experimentally observed phenomena was captured.

Acknowledgments

This work was supported by the Semiconductor Research Corp., National Science Foundation (CTS 99-74962), Novellus Inc., Applied Materials Inc. and LSI Logic.

References

[1] Carter C and Khachan J 1999 *Plasma Source Sci. Technol.* **8** 432
[2] Kim S S, Chang S C, Yoon S N and Whang K 1999 *Phys. Plasmas* **6** 2926
[3] Shamrai P K and Taranov B V 1996 *Plasma Source Sci. Technol.* **5** 474
[4] Boswell W R and Chen F F 1997 *Trans. Plasma Sci.* **25** 1229
[5] Chen F F and Boswell W R 1997 *Trans. Plasma Sci.* **25** 1245
[6] Shamrai P K 1998 *Plasma Source Sci. Technol.* **7** 499
[7] Mouzouris Y and Scharer E J 1998 *Phys. Plasmas* **5** 4253
[8] Arnush D 2000 *Phys. Plasmas* **7** 3042
[9] Borg G G and Boswell W R 1998 *Phys. Plasmas* **5** 564
[10] Chen F F and Blackwell D D 1999 *Phys. Rev. Lett.* **82** 2677
[11] Keiter P A, Scime E E and Balkey M M 1997 *Phys. Plasmas* **4** 2741
[12] Kwak G J, Choi D H, Bak I H, Cho S, Bak G J and Kim K S 1997 *Plasmas* **4** 1463
[13] Kline L J, Scime E E, Boivin F R, Keese M A, Sun X and Mikhailenko V S 2002 *Phys. Rev. Lett.* **88** 195002
[14] Cho S 2000 *Phys. Plasmas* **7** 417
[15] Lieberman A M and Lichtenberg J A 1994 *Principles of Plasma Discharges and Materials Processing* (New York: Wiley)
[16] Ellingboe R A and Boswell W R 1996 *Phys. Plasmas* **3** 2797
[17] Ellingboe R A 1998 Waves and power deposition in a magento-plasma *PhD Thesis* Australian National University
[18] Chen F F and Arnush D 1997 *Phys. Plasmas* **4** 3411
[19] Kinder L R and Kushner J M 2001 *J. Vac. Sci. Technol.* A **19** 76
[20] Kinder L R and Kushner J M 2001 *J. Appl. Phys.* **90** 3699
[21] Freynd W R and Nachtigal M N 1994 *Siam J. Scientific Comput.* **15** 313
[22] Borg G G and Kamenski V I 1997 *Phys. Plasmas* **4** 529
[23] Degeling W A and Boswell W R 1997 *Phys. Plasmas* **4** 2748
[24] Molvik W A, Ellingboe R A and Rognlien D T 1997 *Phys. Rev. Lett.* **79** 233
[25] Rauf S and Kushner J M 1997 *J. Appl. Phys.* **82** 2806
[26] Degeling W A, Jung O C, Boswell W R and Ellingboe R A 1996 *Phys. Plasmas* **3** 2788
[27] Schneider P T, Dostalik W W, Springfield D A and Kraft R 1999 *Plasma Source Sci. Technol.* **8** 397
[28] Tynan R G *et al* 1997 *J. Vac. Sci. Technol.* A **15** 2885
[29] Chen F F 1992 *J. Vac. Sci. Technol.* A **10** 1389
[30] Arnush D and Chen F F 1998 *Phys. Plasmas* **5** 1239
[31] Kamenski I V and Borg G G 1998 *Comput. Phys. Commun.* **113** 10
[32] Enk Th and Krämer M 2000 *Phys. Plasmas* **7** 4308
[33] Shamrai K P and Shinohara S 2001 *Phys. Plasmas* **8** 4659
[34] Carter M D *et al* 2002 *Phys. Plasmas* **9** 5097